ELSEVIER

Contents lists available at ScienceDirect

### Journal of Materials Research and Technology

journal homepage: www.elsevier.com/locate/jmrt





# Assessing residual stress and high-temperature mechanical performance of laser-welded P91 steel for fusion power plant components

Bin Zhu <sup>a</sup> <sup>0</sup>, Omar Mohamed <sup>a</sup> <sup>0</sup>, Abdalrhaman Koko <sup>b</sup> <sup>0</sup>, Hannah Zhang <sup>b</sup>, Jiří Dluhoš <sup>c</sup>, Yiqiang Wang <sup>d</sup>, Michael Gorley <sup>d</sup>, Mark J. Whiting <sup>a</sup> <sup>0</sup>, Tan Sui <sup>a,b,\*</sup> <sup>0</sup>

- <sup>a</sup> School of Engineering, University of Surrey, Guildford, Surrey, GU2 7XH, UK
- <sup>b</sup> National Physical Laboratory, Hampton Road, Teddington, TW11 OLW, UK
- c TESCAN ORSAY HOLDING, a.s., Libušina třída 21, 623 00, Brno, Czech Republic
- d United Kingdom Atomic Energy Authority, Culham Centre for Fusion Energy, Culham Science Centre, Abingdon, Oxon, OX14 3DB, UK

#### ARTICLE INFO

Handling editor: L Murr

Keywords: Laser-welded P91 joints Deformation mechanisms Residual stress PFIB-DIC Nanoindentation

#### ABSTRACT

Residual stress poses significant risks to the life management of key engineering components in nuclear fusion reactors. It is often induced within the narrow heat-affected zone (HAZ) during remote laser welding, essential for maintaining and assembling in-vessel components. Residual stress interacts with high temperatures, degrading mechanical properties and altering fracture mechanisms. Establishing a correlative methodology with microstructures to investigate these stresses and understand their effects on mechanical properties within the narrow HAZ is crucial for extending the reactor's lifetime. In this study, advanced residual stress measurements, including plasma-focused ion beam and digital image correlation, were employed to reveal heterogeneous stress distribution, discovering the peak tensile residual stress of 150 MPa at the interface of the fusion zone (FZ) and HAZ, and peak compressive residual stress of 550 MPa within HAZ. The residual stress effects on micro-hardness are quantitatively evaluated, showing a 25% hardening effect at HAZ/BM interface and a 10% softening effects at fusion line. The deformation mechanism is further analysed using tensile testing, where the residual stress effects were prominent in the low-stress field, reducing 6.5% strain evolution, while microstructures reinforced the material in the high-stress field. At elevated temperatures, the joint exhibited a significant reduction from 532 MPa to 345 MPa for yield strength and from 12 % to 8 % for elongation, with distinct fracture mechanisms observed through fractography compared to its behaviour at room temperature. These findings provide critical insights into enhancing laser welding processing and maintaining the structural integrity of in-service nuclear fusion reactor components.

#### 1. Introduction

To solve the relentless increase in energy demands and the consequential rise of energy-related emissions, a shift towards sustainable, clean energy production is imperative. Nuclear fusion is an attractive option to meet this demand and, if realised, provide an abundance of benefits unmatched by other solutions currently being explored. The necessary technologies not only concern robust plasma control but also include structural integrity of the plant for reliable and cost-effective electricity generation. The in-vessel components in the fusion/fission plant such as pipes for heat exchangers and helium and coolants, have to utilise complicated joining techniques, such as remote laser welding [1–3], to maintain their function under high-temperature operating

conditions, up to 650 °C [4–7]. However, substantial microstructural changes and induced heterogeneous residual stress after welding processes notably degrade the mechanical properties of the weldment [8,9]. Such effect can be more sophisticated, rendering the mechanical properties unpredictable at the high operating temperature. Therefore, to optimise the laser welding processing for the structural integrity of the nuclear fusion reactor components, it is critical to establish a methodology to quantitatively evaluate the residual stress and material strength, and correlate with deformation mechanism.

The methodology is investigated based on the P91 steel, denoted ASTM A335 for plate and T91 for tubing, which is renowned for its excellent high-temperature weldability and microstructural stability, in particular, high-temperature creep resistance for extensive periods [10].

<sup>\*</sup> Corresponding author. School of Engineering, University of Surrey, Guildford, Surrey, GU2 7XH, UK. *E-mail address*: t.sui@surrey.ac.uk (T. Sui).

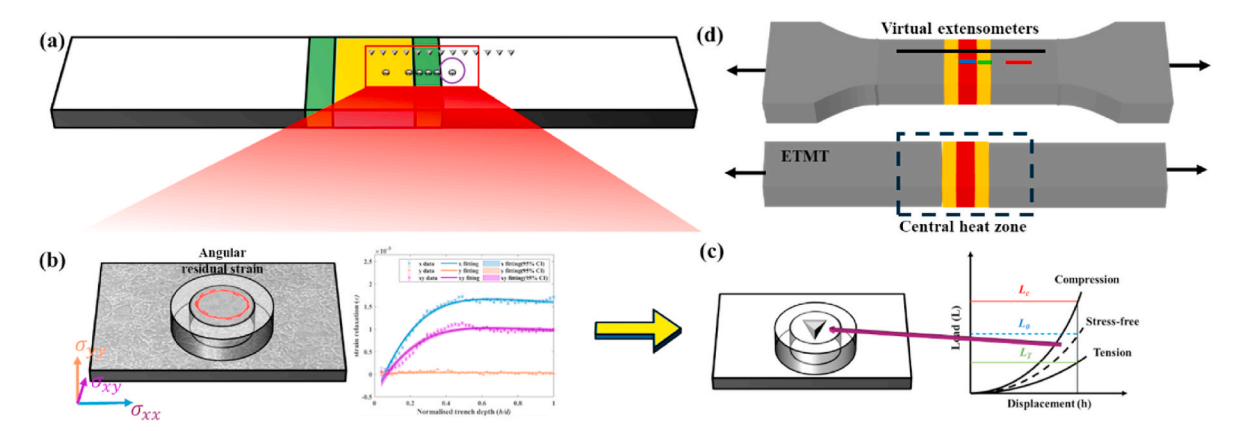


Fig. 1. (a) Laser-welded P91 specimen for residual stress, microstructures (EBSD and SEM) and micro-hardness characterisation, (b) the PFIB-DIC ring-core residual stress quantification, (c) the nanoindentation residual stress measurement, where the ring-core fabricated during PFIB-DIC measurement provides a stress-free reference, (d) the dog-bone specimen used in the room temperature uniaxial tensile test and virtual extensometers applied in DIC analysis, andthe rectangular sample for high-temperature tensile testing using the electro-thermal mechanical testing.

The laser-welding process induces the narrow Fusion Zone (FZ), Heat-Affected Zone (HAZ), Base Material (BM). Accurately evaluating residual stress distribution in these narrow welding sub-regions is remarkably important for the establishment of the methodology, which requires reliable measurements within a few hundred micrometres length-scale. Current residual stress measurements at the microscale includes lab-based and synchrotron-based X-ray diffraction techniques that usually require thin sample dimensions due to their intrinsic penetration limitation [11-14]. The residual stress leans towards releasing during the thin sample preparation, resulting in unexpected uncertainties. Whilst the residual stress evaluation for similar or dissimilar P91 joints has been primarily conducted using the contour method, neutron diffraction and finite element analysis technique at a millimetre scale [15-20], the residual stress on a finer scale, which is profound in correlating the heterogeneous mechanical properties for the narrow sub-regions of the laser-welded P91 joint, has not been revealed.

The lack of such finer-scale residual stress evaluation led to the insufficient deformation mechanism analysis on laser-welded P91 joint, hindering the optimisation of the welding processing. For example, several studies have been achieved on analysing the mechanistic connection of microstructures with micro-hardness distribution and tensile strength [21–25]. The change of the micro-hardness has been only correlated with hardening effects of recrystallisation, precipitates and martensitic phase transformation originated from high heat input during laser welding. Similarly, using digital image correlation to monitor the strain evaluation during tensile deformation allows the study of tensile behaviour in local sub-regions and builds correlation with localised microstructures [26,27]. However, the heterogeneous residual stress, which can have a profound effect on the mechanical properties, has been overlooked for a comprehensive deformation mechanism within the laser-welded P91 joints.

This study addresses a key gap by developing a methodology for correlatively analysing residual stress, microstructures, and mechanical properties in P91 joints, offering valuable insights to optimise laser-welding processes. Using a novel tunable-scale residual stress evaluation technique, Plasma Focused Ion Beam Combined and Digital Image Correlation (PFIB-DIC), the research quantifies residual stress across narrow sub-regions of laser-welded P91 joints, advancing precision in residual stress assessment [28]. Instrumented nanoindentation was also used to cross-validate the residual stress distribution and characterise the micro-hardness. The microstructural changes over the weldment are then observed by the Electron Backscatter Diffraction (EBSD) and the local heterogenous tensile strain evolution in different sub-regions is characterised by the DIC at room temperature. The influence of heterogeneous microstructural and residual stress distribution on

mechanical properties is quantitatively analysed with respect to the micro-hardness and tensile strength difference in FZ, HAZ and BM regions. Additionally, this study has extended the correlative methodology to the in-service temperature of 550 °C, typical for nuclear fusion reactor. The failure mechanism was investigated via the comparison of the fractography at room and elevated temperatures. The experimental data can be directly utilised for validating finite element simulations, which can generate additional data to establish data-driven machine learning (ML) models [3]. Furthermore, understanding deformation mechanisms helps establish physical constraints for developing physics-informed ML models, providing insights into the optimisation of the welding processing for producing the long lifespan fusion power plant components.

#### 2. Materials and methods

#### 2.1. Materials and microstructure characterisation

The P91 steel with a composition Fe-0.12C-8.32Cr-1.02Mo-0.41Mn-0.24 V (weight %) was used in the present investigation. The as-received 6-mm-thick P91 steel plate was normalised at 1050 °C, and water quenched to room temperature followed by tempering at 760 °C for 3 h then cooled in the air [24]. Two as-received P91 steel plates, each 150  $\times$  $75 \times 6 \text{ mm}^3$ , were butt welded perpendicular to the rolling direction by laser welding. The single-pass laser welding used a 5 kW Yb-fibre laser source with a welding speed of 1.2 m/min and was manufactured by TWI. The process enabled full penetration, a narrow FZ and HAZ, and resulted in a slightly concave weldment. As shown in Fig. 1(a), the laser-welded P91 specimen used in this research was cut from the laser-welded P91 plate by electrical discharge machining with the dimension of  $\sim 25 \times 6 \times 6$  mm<sup>3</sup>. Based on previous experiment, the residual stress is retained after cutting at the measurement scale and suitable for the microscopy-based evaluation techniques [29]. Microstructural characterisation was carried out on material red box (Fig. 1 (a)) by a Jeol-7100F field emission Scanning Electron Microscopy (SEM), equipped with a Thermo Fisher Lumis EBSD detector. Post-data-treatment was completed with MTEX 5.2.8 [30], and the crystal size was measured by the mean linear intercept method [31]. The material anisotropy in x and y directions, i.e. Young's modulus and Poisson coefficient, was reckoned according to the crystal orientation.

## 2.2. Residual stress measurement using plasma focused ion beam and digital image correlation

The PFIB-DIC ring-core method was applied in the FZ, HAZ and BM

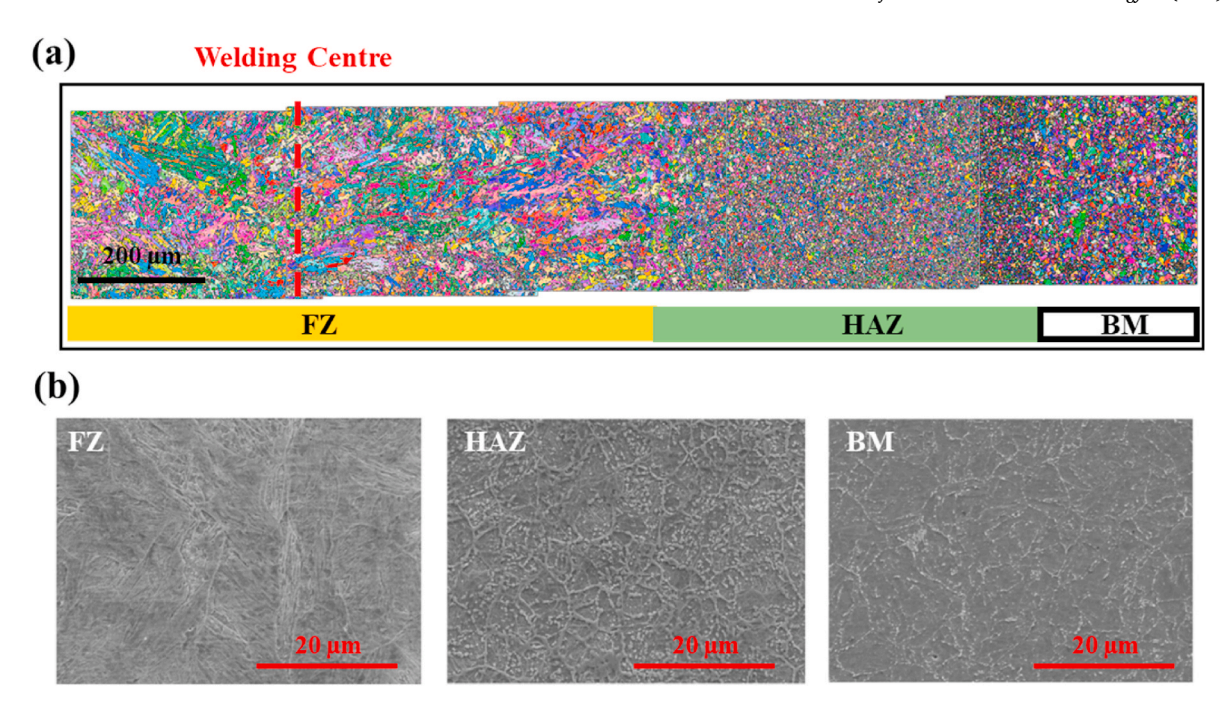


Fig. 2. Microstructure characterisation results. (a) Stitched consecutive EBSD orientation maps highlighted by the rectangle in red at Fig. 1(a), (f) SEM images showing the difference in microstructure of the FZ, HAZ and BM regions.

regions, as well as the interface of FZ/HAZ and HAZ/BM (Fig. 1(a)) to assess the non-equi-biaxial residual stresses because it allows simultaneous evaluation of three components of in-plane normal and shear strain relaxation ( $\Delta \varepsilon_x$ ,  $\Delta \varepsilon_y$  and  $\Delta \varepsilon_{xy}$ ), as shown in Fig. 1(b) [28]. Considering anisotropic properties of ring-cores, the residual stresses in the x and y directions was calculated using the generalised Hooke's law (Eq. (1) and Eq. (2)) [28,32].

$$\sigma_x^{p_{FIB}} = -rac{E_x}{(1-
u_x
u_y)}igg[\Delta\Big(\Deltaarepsilon_x+
u_x\Deltaarepsilon_yigg]$$
 Eq. 1

$$\sigma_y^{PFIB} = -rac{E_y}{(1-
u_x
u_y)}igg[\Delta\Big(\Deltaarepsilon_x+
u_y\Deltaarepsilon_yigg]$$
 Eq. 2

where and  $\sigma_x^{PFIB}$  and  $\sigma_y^{PFIB}$  are two in-plane residual stress components in x and y directions.  $E_x$ ,  $E_y$ ,  $v_x$ , and  $v_y$  are Young's moduli and Poisson coefficients computed according to the crystal orientation in the ringcore area in x and y directions, respectively.

The derivation of the full strain relief in three different directions enables direct calculation of the principle strain relief values ( $\varepsilon_{1.2}^{\rm PFIB}$ ) and orientation using Mohr's circle via Eq. (3) and Eq. (4) [32,33]. Then the principal residual stress ( $\sigma_1^{\rm PFIB}$  and  $\sigma_2^{\rm PFIB}$ ) obtained from PFIB-DIC method can be calculated using Eq. (5) and Eq. (6), where the  $E_{\theta}$  and  $\nu_{\theta}$  is the Young's modulus and Poisson coefficients at the angle  $\theta$ .

$$\varepsilon_{1,2}^{\text{PFIB}} = \frac{\Delta \varepsilon_{x} + \Delta \varepsilon_{y}}{2} \pm \frac{1}{\sqrt{2}} \sqrt{\left(\Delta \varepsilon_{x} - \Delta \varepsilon_{xy}\right)^{2} + \left(\Delta \varepsilon_{xy} - \Delta \varepsilon_{y}\right)^{2}}$$
 Eq. 3

$$\theta = \frac{1}{2} tan^{-1} \left( \frac{\Delta \varepsilon_x - 2\Delta \varepsilon_{xy} + \Delta \varepsilon_y}{\Delta \varepsilon_x - \Delta \varepsilon_y} \right)$$
 Eq. 4

$$\sigma_1^{ ext{PFIB}} = -rac{E_ heta}{(1-
u_ heta)} \left( arepsilon_1^{ ext{PFIB}} + 
u_ heta arepsilon_2^{ ext{PFIB}} 
ight)$$
 Eq. 5

$$\sigma_2^{\text{PFIB}} = -\frac{E_{\theta}}{(1-\nu_{\theta})} \left( \varepsilon_2^{\text{PFIB}} + \nu_{\theta} \varepsilon_1^{\text{PFIB}} \right) \tag{Eq. 6}$$

#### 2.3. Residual stress measurement using nanoindentation

The schematic in Fig. 1(c) shows how nanoindentation is used to measure the residual stress in the weldment by comparing the loaddisplacement curve with the stress-free reference obtained from the ring-core regions. The classical symmetric pyramid or spherical indenter tip limits the use of nanoindentation in non-equi-biaxial residual stress states. Using the PFIB-DIC technique allows the determination of a preknown stress ratio between two principal residual stress components  $(\sigma_1^{PFIB})$  and  $\sigma_2^{PFIB}$  to estimate non-equi-biaxial residual stress via Lee's model [28,34,35]. The high-resolution stress ratio was gained from PFIB-DIC measurements with  $k=rac{\sigma_p^{PFIB}}{\sigma_p^{PFIB}},$  where -1 < k < 1 and k 
eq 0.The line-scan was performed across the weldment for residual stress and micro-hardness characterisation, as shown in Fig. 1(a). Displacement control with 1 µm/min was used to carry out the indentation using Ultra Indentation Tester, and data was acquired at depths of 500 nm and 1000 nm. The area function of the Berkovich indenter was calibrated against the certified reference material. The Micro-hardness is determined according to the Oliver and Pharr theory [36].

#### 2.4. Mechanical testing at room and elevated temperatures

The samples for tensile testing, including dog-bone and rectangular shapes, were cut by electrical discharge machining from the same laserwelded P91 plate. The uniaxial room temperature tensile was conducted using a universal material testing machine (Instron 5500). The deformation was induced in uniaxial tension until failure at a constant displacement rate of 0.02 mm/s, and DIC software (Vic-2D v6, Correlated Solutions, US) [37] was used to visualise the heterogeneous strain distribution throughout the tensile deformation. The tensile response was measured by multiple virtual extensometers, as shown in Fig. 1(d). The high-temperature tensile testing was carried out using the electro-thermal mechanical testing. A R-type thermocouple was affixed to the centre heat zone of the sample Fig. 1(d)), which is in the dimension  $3 \times 1 \times 65 \text{ mm}^3$ , for monitoring and controlling the temperature. The temperature of the sample was then elevated to 550 °C at a rate of 5  $^{\circ}\text{C/s}$ , followed by a stabilising period of 2 min. The uniaxial tensile deformation was induced at a displacement rate of 0.02 mm/s

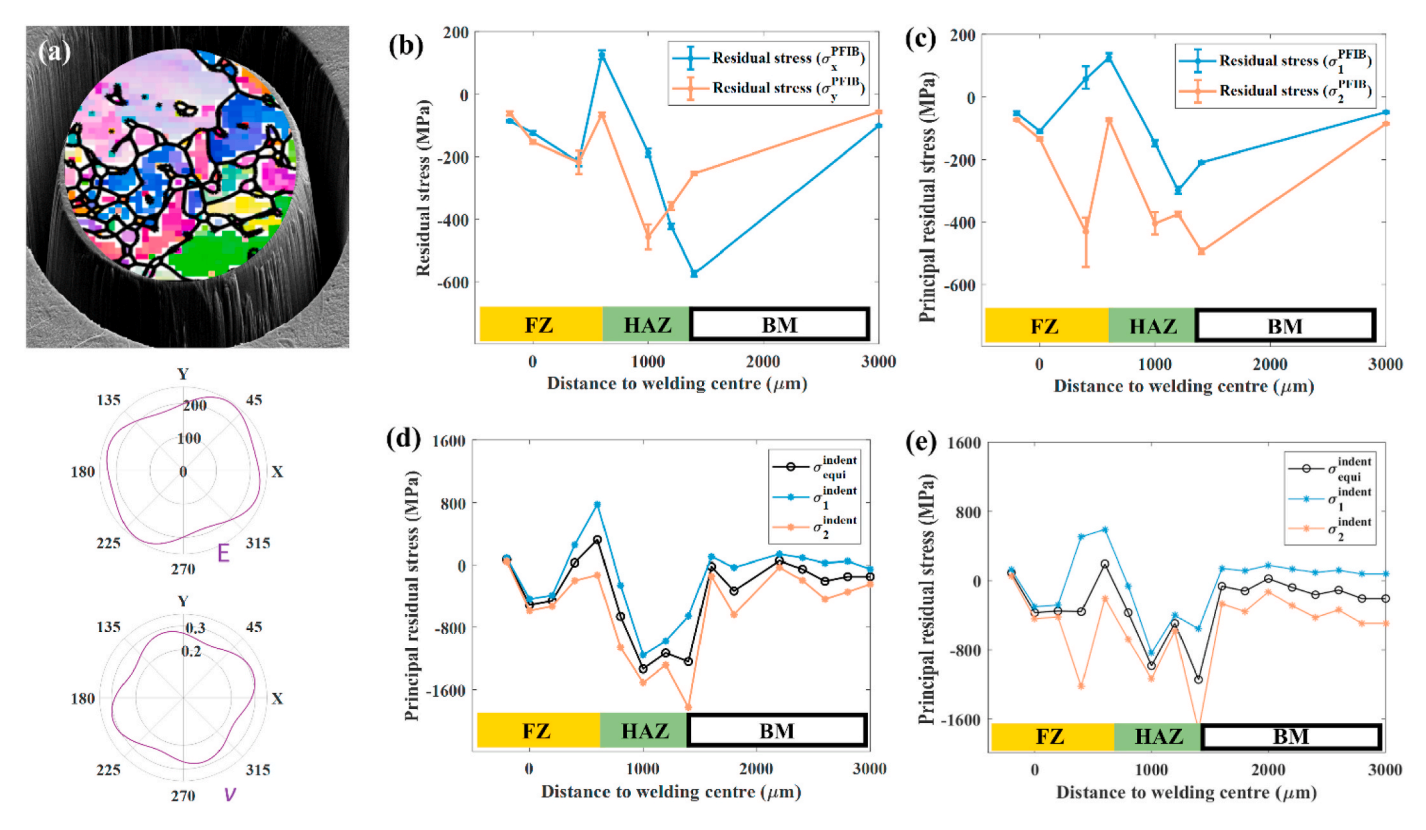


**Fig. 3.** Residual stress characterisation using a PFIB-DIC ring-core method and a nanoindentation technique which accounts for anisotropy. (a) EBSD orientation map of the crystal orientation in the ring-core region by which the anisotropy is quantitatively calculated in the *x* and *y* directions, (b) residual stress distribution quantified by PFIB-DIC in the *x* and *y* directions, (c) principal residual stress distribution calculated from PFIB-DIC measurements, (d) principal residual stress distribution analysed at a depth of 500 nm using nanoindentation.

until fracture.

#### 3. Results and discussion

The stitched EBSD orientation maps and morphologies of the FZ, HAZ and BM regions revealed by backscattred electron imaging, see Fig. 2(e and f), show the heterogeneous nature of the microstructure across the weldment. Grain growth is observed in the FZ region, and is most evident close to the fusion line (i.e., FZ/HAZ interface). The grain size decreases dramatically from the FZ to the HAZ, with a slight increase in the BM region. There is no strong evidence of preferred orientation in the EBSD orietation maps. The morphology (Fig. 2 (f)) varied substantially across the weldment, depending on the peak heat input attained during the laser welding. Unlike other welding processes,  $\delta$ -ferrite, which is usually seen as an undesirable phase in 9–12% Cr steel, is not observed after laser-welding [38]. The lath martensite with packet boundary was found in both the FZ, and tempered martensite was identified in the HAZ and BM regions.

The PFIB-DIC ring-core method and nanoindentation techniques reveal residual stress distribution and enable correlation of microstructure with mechanical properties. Fig. 3(a) shows an example of extracting the grain microstructures in the ring-core region from the EBSD orientation map. The as-welded P91 steel is assumed to exhibit cubic crystal symmetry, and the elastic constants of reduced activation ferritic/martensitic steel have been studied previously [39]. The anisotropic Young's modulus and Poisson coefficient are computed iteratively at different directions and used to calculate residual stress in the x and y directions via generalised Hooke's law. Fig. 3(b) presents the residual stress distribution quantified by the PFIB-DIC ring-core method in x and y directions. Our findings show the peak magnitude of residual stress is at the FZ/HAZ and HAZ/BM interfaces, where the microstructures change over short length scales. The tensile peak of residual stress

( $\sim$ 150 MPa) is found at the FZ/HAZ interface in the x direction and is balanced by a compressive residual stress on both sides of this interface. The compressive peak ( $\sim$ 550 MPa) is observed the interface of the HAZ and BM. The residual stress gradually decreases away from the weldment. The residual stress distribution in laser-welded P91 is consistent with other similar laser-welded reduced activation ferritic/martensitic joints also measured by the PFIB-DIC ring-core method [28]. The principal residual stresses derived from PFIB-DIC is shown in Fig. 3(c), as  $\sigma_1^{PFIB}$  and  $\sigma_2^{PFIB}$ .

Instrumented nanoindentation has great potential for identifying residual stresses because of the time efficiency, simplicity of use and applicability from nano to macro scales [34,35,40-42]. Fig. 3(d) and (e) show the equi-biaxial principal residual stress distribution ( $\sigma_{equi}^{indent}$ ) extracted at depths of 500 nm and 1000 nm from the nanoindentation measurements. The two depth-resolved residual stress distributions follow a similar shape, while the magnitude is slightly higher at a depth of 500 nm. The stress coefficient (k) established by PFIB-DIC measurement is used to calculate the non-equi-biaxial components ( $\sigma_1^{indent}$  and  $\sigma_2^{indent}$ ) from nanoindentation. The residual stress distribution derived from nanoindentation measurements cross-validate the ones from the PFIB-DIC evaluation, although a discrepancy in magnitude is found, which can be attributed to three factors. Such a difference might be due to the depth sensitivity of the nanoindentation residual stress measurement given its shallow depth. The indentation size effect originates from dislocation density and causes load amplification in the load-displacement curve at a smaller scale [43,44]. The accompanying magnification of residual stress occurs while comparing with the stress-free reference. Although increasing displacement in nanoindentation measurement may extenuate this issue (Fig. 3(e)), there is a risk of pile-up phenomenon in some compressive residual stress areas leading to an error in accounting for contact area. In this case, further

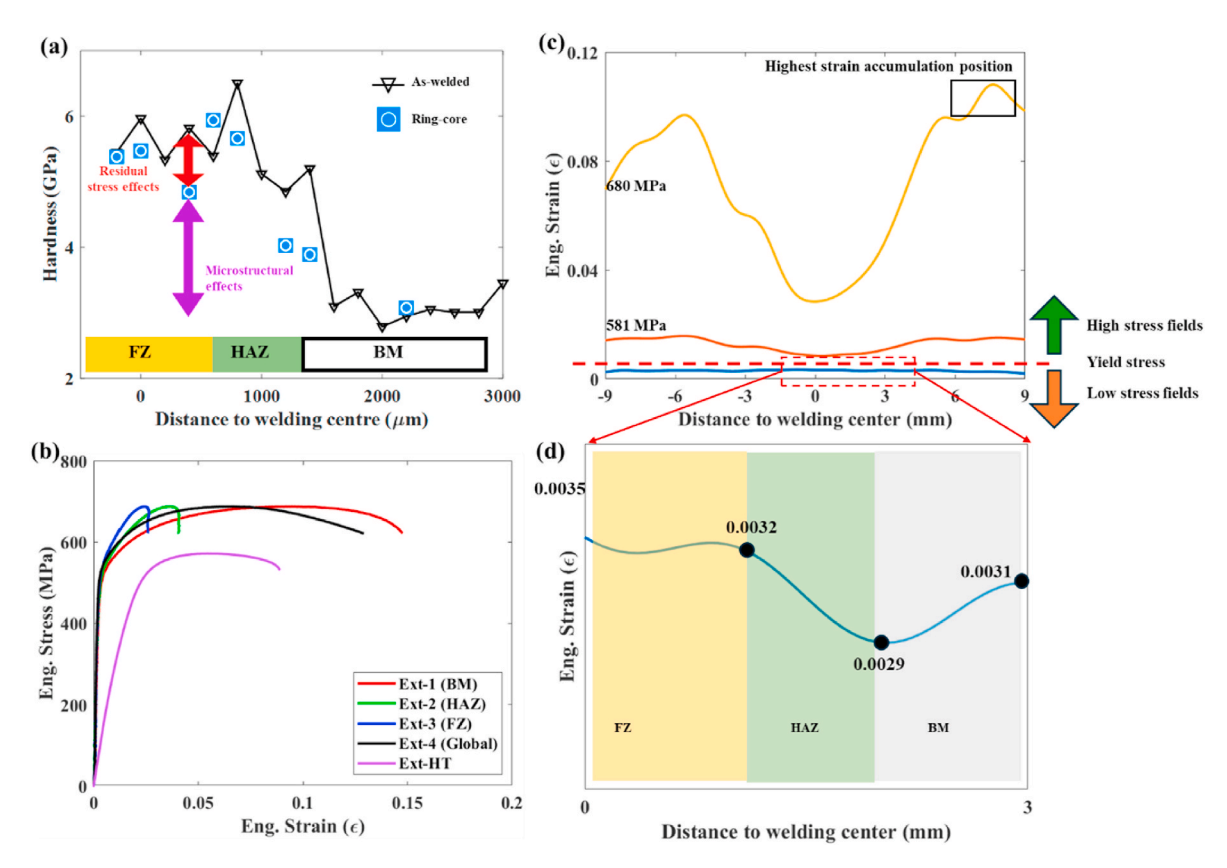


Fig. 4. Mechanical properties of as-welded and stress-free P91 steel at room and high temperatures. (a) Room-temperature evaluation of micro-hardness distribution across the weldment and stress-free ring-cores in the FZ, HAZ and BM regions. (b) Tensile behaviour, at room and high-temperature, of laser-welded P91 joint. (c) The room temperature heterogeneous tensile strain distribution measured by virtual extensometers during the tensile deformation within the FZ, HAZ and BM at low and high stress fields. (d) Zoom-in tensile strain distribution within the low stress field.

evaluation of the contact area might be necessary. In addition, non-equilibrium micro-scale residual stress derived from the local anisotropic properties also contributes to depth effects. Applying multiple or high-depth measurements enables consideration of a larger number of grains, equilibrating the micro-scale residual stress and overcoming this limitation [28].

To study the residual stress effects on mechanical properties, the micro-hardness and tensile behaviour are characterised at room and high temperatures and visualised in Fig. 4. A significant advantage of using nanoindentation is that the micro-hardness and other mechanical properties can be measured in addition to residual stress measurements. Local micro-hardness values are severely affected by the microstructure (e.g. grain size, quenched martensite and precipitates) and the residual stress. The hardest position ( $\sim$ 6.5 GPa) is identified in the HAZ, which is also adjacent to the fusion line (Fig. 4(a)). The micro-hardness gradually and constantly decreases to (~3.1 GPa) until the BM region. The microstructural hardening is concluded by comparing the microhardness of the stress-free reference ring-cores with that of the BM region. As shown in (Fig. 4(a)), the microstructures harden the edge of the FZ region up to  $\sim 5.9$  GPa, which is attributed to the presence of martensite and carbide dissolution during the welding cycle [45]. The grain growth (see Fig. 1(e)) in the FZ region slightly weakens this hardening effect. As the peak temperature decreases, the reduction of a fraction of quenched martensite and residual of coarsen carbides decline the microstructure hardening in the HAZ region. Link to the residual stress distribution, the most apparent tensile principal residual stress is located at the FZ region of the FZ/HAZ interface, which is due to the tensile residual stress tends to appear at the soft area [46,47]. The residual stress effects on micro-hardness is also separated quantitatively by comparing the micro-hardness between the as-welded state and stress-free reference in different regions of the weldment (Fig. 4(a)). The

compressive residual stresses harden the FZ by up to 16% and HAZ/BM interface by 25%, whilst the tensile residual stresses produce a softening effect around the fusion line by 10%. Both residual stress and microstructural hardening effects are diminishing while reaching the BM region, the micro-hardness almost remains the same as the parent materials.

Fig. 4(b) illustrates the tensile behaviour in the loading direction (xdirection), where the fracture occurred at the BM region both at room and high temperatures. The four virtual extensometers covering different sub-regions enables the correlation between residual stress, microstructures, and tensile behaviour at room temperature. As shown in Fig. 4(b), the FZ region shows the highest 0.2% offset yield stress (568 MPa) compared to the HAZ (539 MPa) and BM (504 MPa) regions. Essentially the same stiffness was observed in the elastic regime for all global and sub-regions. As with the micro-hardness (Fig. 4(a)), the FZ region was found to be the region most strengthened by microstructure (i.e. martensite formation during rapid cooling after welding processing and carbide dissolution) and compressive residual stresses, whilst the BM region shows the highest ductility. The HAZ region is strengthened by its fine grain size, the martensitic phase transformation and compressive residual stresses, with the yield strength slightly below the FZ region. At the high temperature, the joint exhibits a yield stress with a 0.2% offset of 345 MPa and an ultimate tensile stress of 568 MPa. In contrast, at room temperature, the yield stress of the joint with a 0.2% offset is approximately 532 MPa, and the ultimate tensile stress is approximately 687 MPa. Compared to room temperature, the weldment demonstrates lower strain elongation, reduced from 12% to 8 %, at elevated temperatures. The similar phenomenon is also found from the P91 joint that welded by other joining techniques [48].

Fig. 4(c) visualises the accumulation of heterogeneous strain distribution crossing different regions of the weldment using the DIC at the

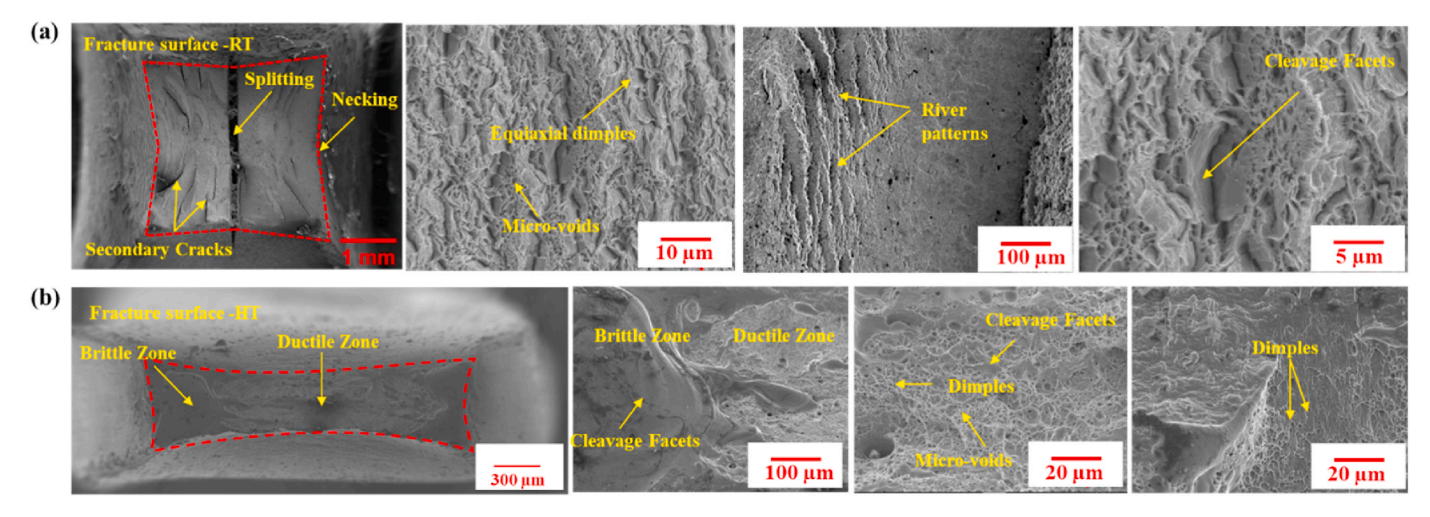


**Fig. 5.** The fracture surfaces were examined by secondary electron imaging following tensile testing at (a) room temperature, and (b) high temperature (550 °C). Typical features include splitting, secondary cracking, necking, dimples, micro(macro)-voids, river patterns and quasi cleavage.

room temperature, where the strain is accumulated in the ductile BM region (highlighted by black box), resulting in a fracture. In the highstress field, the influence of residual stress on strain evolution appears minimum, with microstructural effects predominantly governing the material response. The FZ region exhibits the lowest strain evolution, showing a reduction of over 50% compared to the BM region. Conversely, analysis of tensile behaviour across different weldment regions using DIC suggests that microstructural effects can be neglected in the low-stress field or elastic regime. This conclusion is supported by the similarity in yield strength and stiffness observed in the tensile stressstrain curves. In this context, a closer inspection of the weld region within the low-stress field (Fig. 4 (d)) reveals strain evolution values of 0.0029 at the HAZ/BM interface, 0.0032 at the fusion line, and 0.0031 in the BM. The BM strain evolution serves as a reference for a stress-free region, while variations at the HAZ/BM interface and fusion line are attributed to localised tensile or compressive residual stress. Given the small strain evolution in the elastic deformation regime, the highest compressive residual stress at the HAZ/BM interface reduces strain evolution by 6.5%, while the tensile residual stress at the fusion line slightly increases tensile strain evolution by 3.2%.

At room temperature, a mixed mode of ductile and brittle fracture is evident, see Fig. 5(a). The ductile zones have the typical micro-voids and equiaxial dimples which are evidence of extensive plasticity leading to void formation, their coalescence and eventual fracture. Large areas of quasi-cleavage facets are observed with river patterns, which are typical characteristics of transgranular brittle fracture [49]. The splitting and secondary cracking observed (Fig. 5(a)), have been explained as decohesion of the interface between lath ferrite-lath matrix and secondary precipitates [50-52]. At high temperature, the mix fracture mode is observed, as depicted in Fig. 5(b), where the fracture surface exhibits ductile features, including dimples and micro- and macro-voids. The loss of strength may lead to the rapid deformation to form the cleavage facets in the brittle zone, ultimately reducing its capacity to undergo elongation before failure. In contrast to the room temperature fracture, which shows some cleavage features, the high-temperature fracture surface displays limited cleavage features within the brittle zone of the fracture surface but none of river patterns, indicating a more ductile response. In addition, no secondary cracking is observed at moderate elevated temperature. This is also in good agreement with the stress-strain response (Fig. 4(b)) where higher ductility and lower stiffness are observed.

#### 4. Conclusion

This work has established the deformation mechanisms of laser-

welded P91 joints by considering the effect of both heterogeneous residual stress and localised microstructures. The residual stress distribution across the narrow sub-regions of the joints was quantified and crossvalidated, where the peak residual tensile stress (~150 MPa) is found in the loading direction at the FZ/HAZ interface, balanced by compressive residual stress (~550 MPa) within the HAZ. The effects of residual stress are quantified via the micro-hardness, where the residual stress contribute to up to 16% to the material hardening in the FZ and 25% of materials hardening at the HAZ/BM interface. A similar strengthening phenomenon is observed under tension, where residual stress effects dominate in low-stress regions, while microstructural strengthening plays a dominant role in high-stress regions. Compared to the BM region, compressive residual stress at the HAZ/BM interface reduces strain evolution by 6.5% in low-stress regions, whereas tensile residual stress increases strain evolution at the FZ/HAZ interface by 3.2%. At 550 °C, weldment softening occurs, with yield strength decreasing from 532 MPa to 345 MPa, ultimate tensile stress dropping from 687 MPa to 568 MPa, and elongation reducing from 12% to 8%. This observation is consistent with the fractographic analysis, which shows a brittle-ductile mix mode features at elevated temperatures.

#### Declaration of competing interest

The authors declare that they have no known competing financial interests or personal relationships that could have appeared to influence the work reported in this paper.

#### Acknowledgements

Dr Wang and Dr Gorley would like to acknowledge the Engineering and Physical Sciences Research Council (EPSRC) Energy Programme, grants number EP/W006839/1 and the Department for Energy Security and Net Zero. Dr Sui would like to acknowledge funding from the Royal Academy of Engineering under the Industrial Fellowships programme. Part of this work was supported by grants from the EPSRC project (EP/P001521/1). Dr Zhang would like to thank the National Measurement System Programme of the UK Government Department for Business, Energy and Industrial Strategy for financial support.

#### References

- Kirk S, Suder W, Keogh K, Tremethick T, Loving A. Laser welding of fusion relevant steels for the European DEMO. Fusion Eng Des 2018. https://doi.org/10.1016/j. fusengdes.2018.03.039.
- Buckingham R, Loving A. Remote-handling challenges in fusion research and beyond. Nat Phys 2016;12. https://doi.org/10.1038/nphys3755.

- [3] Zhu B, Leung N, Steel B, England D, He Y, London AJ, et al. Machine learning powered predictive modelling of complex residual stress for nuclear fusion reactor design. Mater Des 2024;248:113449. https://doi.org/10.1016/
- [4] Lässer R, Baluc N, Boutard JL, Diegele E, Dudarev S, Gasparotto M, et al. Structural materials for DEMO: the EU development, strategy, testing and modelling. Fusion Eng Des 2007;82:511–20. https://doi.org/10.1016
- [5] Kirk S, Suder W, Keogh K. Laser Welding of P91 & EUROFER97 steels for fusion reactor coolant pipes. https://doi.org/10.13140/RG.2.2.26630.16967; 2016.
- [6] Pintsuk G, Aiello G, Dudarev SL, Gorley M, Henry J, Richou M, et al. Materials for in-vessel components. Fusion Eng Des 2022;174:112994. https://doi.org/10.101
- [7] Anderton MD, Baus C, Davis TP, Pearson R, Mukai K, Pollard J, et al. Novel high temperature tritium blanket designs for confined spaces in spherical tokamak fusion reactors. Fusion Eng Des 2025;210:114732. https://doi.org/10.1016/j
- [8] Withers PJ. Residual stress and its role in failure. Rep Prog Phys 2007;70:2211-64. https://doi.org/10.1088/0034-4885/70/12/R04.
- Wang Y, Kannan R, Li L. Insight into Type IV cracking in Grade 91 steel weldments. Mater Des 2020;190:108570. https://doi.org/10.1016/j.matdes.2020.108570
- [10] Lakshmanan V, Arunnellaiappan T, Sathiya P. Microstructural characterization of dissimilar laser beam welded joints between Incoloy 800HT and P91 steel. Int J Pres Ves Pip 2025;214:105408. https://doi.org/10.1016/j.ijpvp.2024.10540
- [11] Yildirim C, Jessop C, Ahlström J, Detlefs C, Zhang Y. 3D mapping of orientation variation and local residual stress within individual grains of pearlitic steel using synchrotron dark field X-ray microscopy. Scr Mater 2021;197:113783. https://doi. g/10.1016/j.scriptamat.2021.11378
- [12] Chen W, Voisin T, Zhang Y, Florien J-B, Spadaccini CM, McDowell DL, et al. Microscale residual stresses in additively manufactured stainless steel. Nat Commun 2019;10. https://doi.org/10.1038/s41467-019-12265-8
- Withers PJJ, Bhadeshia HKDH. Residual stress. Part 1 measurement techniques. Mater Sci Technol 2013;17:355-65. https://doi.org/10.1179/
- [14] Sisodia RPS, Gigli L, Plaisier J, Mertinger V, Weglowski M St, Sliwinski P. Synchrotron diffraction residual stresses studies of electron beam welded high strength structural steels. J Mater Res Technol 2024;30:6291–300. https://doi.org/ 10.1016/j.jmrt.2024.04.240.
- [15] Paddea S, Francis JA, Paradowska AM, Bouchard PJ, Shibli IA. Residual stress distributions in a P91 steel-pipe girth weld before and after post weld heat treatment. Mater Sci Eng 2012;534:663–72. https://doi.org/10.1016/j msea.2011.12.024
- [16] Kundu A, Bouchard PJ, Kumar S, Venkata KA, Francis JA, Paradowska A, et al. Residual stresses in P91 steel electron beam welds. Sci Technol Weld Join 2012;18. https://doi.org/10.1179/1362171812Y.0000000076.
- Yaghi AH, Hyde TH, Becker AA, Sun W. Finite element simulation of welding and residual stresses in a P91 steel pipe incorporating solid-state phase transformation and post-weld heat treatment n.d. https://doi.org/10.1243/03093247JSA372
- [18] Kumar S, Kundu A, Venkata KA, Evans A, Truman CE, Francis JA, et al. Residual stresses in laser welded ASTM A387 Grade 91 steel plates. Mater Sci Eng 2013;575: 160-8 https://doi.org/10.1016/j.msea.2013.03.046
- Javadi Y. Smith MC, Abburi Venkata K. Naveed N. Forsey AN, Francis JA, et al. Residual stress measurement round robin on an electron beam welded joint between austenitic stainless steel 316L(N) and ferritic steel P91. Int J Pres Ves Pip 2017;154:41–57. https://doi.org/10.1016/j.ijpvp.2017.06.002.
  [20] Zubairuddin M, Vasudevan M, Elumalai PV, Akram M, Attar PR, Krishnasamy E.
- Numerical and experimental analysis of temperature and residual stress of GTA and LASER welding for grade 91 steel. Int J Interact Des Manuf 2024. https://doi.org/ 10.1007/s12008-024-02138-
- [21] Zhang S, Melfi T, Narayanan BK. Effects of precipitates on mechanical properties of P91 submerged arc welds. Sci Technol Weld Join 2016. https://doi.org/10.117 362171815Y 0000000076
- [22] Vidyarthy RS, Dwivedi DK. Microstructural and mechanical properties assessment of the P91 A-TIG weld joints. J Manuf Process 2018;31. https://doi.org/10.1016/j. mapro.2017.12.012.
- [23] Bi T, Deng D, Tong Y, Liu X, Zhou Y. Investigation of influence of phase transformation on welding residual stress in P91 steel. Proceedings of the WSE2013, 2013.
- [24] Ruiz-Moreno A, Hähner P, Fumagalli F, Haiblikova V, Conte M, Randall N. Stress-strain curves and derived mechanical parameters of P91 steel from spherical nanoindentation at a range of temperatures. Mater Des 2020;194: 108950. https://doi.org/10.1016/j.matdes.2020.108950.
- [25] Sauraw A, Sharma AK, Fydrych D, Sirohi S, Gupta A, Świerczyńska A, et al. Study on microstructural characterization, mechanical properties and residual stress of GTAW dissimilar joints of P91 and P22 steels. Materials 2021;14. https://doi.org/ 10.3390/ma14216591.
- [26] Park HK, Ameyama K, Yoo J, Hwang H, Kim HS. Additional hardening in harmonic structured materials by strain partitioning and back stress. Mater Res Lett 2018;6. s://doi.org/10.1080/21663831.2018.1439115.
- [27] Ahn J, Chen L, He E, Davies CM, Dear JP. Effect of filler metal feed rate and composition on microstructure and mechanical properties of fibre laser welded AA 2024-T3. J Manuf Process 2017;25:26-36. https://doi.org/10.1016/j. imapro, 2016, 10, 006,

- [28] Bin Z, Yiqiang W, Jiří D, J LA, Michael G, J WM, et al. A novel pathway for multiscale high-resolution time-resolved residual stress evaluation of laser-welded Eurofer97. Sci Adv 2022;8:eabl4592. https://doi.org/10.1126/sciadv.abl45
- [29] Zhu B, Wang Y, Dluhoš J, London AJ, Gorley M, Whiting MJ, et al. A novel pathway for multiscale high-resolution time-resolved residual stress evaluation of laser-welded Eurofer97. Sci Adv 2022;8. https://doi.org/10.1126/sciadv.abl4592.
- Mainprice D, Hielscher R, Schaeben H. Calculating anisotropic physical properties from texture data using the MTEX open-source package. Geol Soc Spec Publ 2011; 360:175–92. https://doi.org/10.1144/SP360.10.
- Roebuck B, Bennett EG, Dickson A. The measurement of uncertainty in grain size distribution, Interlaboratory exercise part 1-reference images, National Physical
- [32] Salvati E, Sui T, Korsunsky AM. Uncertainty quantification of residual stress evaluation by the FIB-DIC ring-core method due to elastic anisotropy effects. Int J Solids Struct 2016;87:61-9. https://doi.org/10.1016/j.ijsolstr.2016.02.0
- [33] Lunt AJGG, Korsunsky AM. A review of micro-scale focused ion beam milling and digital image correlation analysis for residual stress evaluation and error estimation. Surf Coat Technol 2015;283:373-88. https://doi.org/10.1016/j surfcoat, 2015, 10, 049.
- [34] Lee YH, Kwon D. Measurement of residual-stress effect by nanoindentation on elastically strained (1 0 0) W. Scr Mater 2003;49:459-65. https://doi.org/ 10.1016/S1359-6462(03)00290-2
- [35] Lee YH, Kwon D. Estimation of biaxial surface stress by instrumented indentation with sharp indenters. Acta Mater 2004;52:1555-63. https://doi.org/10.1016/j
- [36] Pharr GM. An improved technique for determining hardness and elastic modulus using load and displacement sensing indentation experiments. J Mater Res 1992;7: 1564-83. https://doi.org/10.1557/JMR.1992.1564.
- [37] Student REU, Cintr R, Mentor REU, Saouma V, Rico P, Summer B. Strain measurements with the digital image correlation System vic-2D. System 2008;;106.
- [38] Manugula VL, Rajulapati Kv, Reddy GM, Rao KBS. Role of evolving microstructure on the mechanical properties of electron beam welded ferritic-martensitic steel in the as-welded and post weld heat-treated states. Mater Sci Eng 2017;698. https:// doi.org/10.1016/j.msea.2017.05.036.
- [39] Wang L, Li M, Almer J. Investigation of deformation and microstructural evolution in Grade 91 ferritic-martensitic steel by in situ high-energy X-rays. Acta Mater 2014;62:239-49. https://doi.org/10.1016/j.actamat.2013.10.003
- Suresh S, Giannakopoulos AE. A new method for estimating residual stresses by instrumented sharp indentation. Acta Mater 1998;46:5755-67. https://doi.org 10.1016/S1359-6454(98)00226-2
- [41] Greco A, Sgambitterra E, Furgiuele F. A new methodology for measuring residual stress using a modified Berkovich nano-indenter. Int J Mech Sci 2021;207. https:// doi.org/10.1016/j.iimecsci.2021.106662.
- [42] Moon JH, Baek SM, Lee SG, Seong Y, Amanov A, Lee S, et al. Effects of residual stress on the mechanical properties of copper processed using ultrasonicnanocrystalline surface modification. Mater Res Lett 2019;7:97–102. https://doi. org/10.1080/21663831.2018.1560370.
- [43] Ma X, Higgins W, Liang Z, Zhao D, Pharr GM, Xie KY. Exploring the origins of the indentation size effect at submicron scales. Proc Natl Acad Sci U S A 2021:118. https://doi.org/10.1073/pnas.2025657118.
- [44] Haušild P. On the breakdown of the Nix-Gao model for indentation size effect. Philos Mag 2021;101:420-34. https://doi.org/10.1080/14786435.2020.1841916.
- [45] Cerjak H, Mayr P. Creep strength of welded joints of ferritic steels. Creep-resistant steels. Elsevier; 2008. p. 472-503. https://doi.org/10.1533/ 9781845694012.2.472
- [46] Abburi Venkata K, Truman CE, Coules HE, Warren AD. Applying electron backscattering diffraction to macroscopic residual stress characterisation in a dissimilar weld. J Mater Process Technol 2017;241. https://doi.org/10.1016/j. matprotec, 2016, 11,003
- [47] Raath ND, Norman D, McGregor I, Dashwood R, Hughes DJ. Effect of weld schedule on the residual stress distribution of boron steel spot welds. Metall Mater Trans 2017;48:2900-14. https://doi.org/10.1007/s11661-017-4079-9
- Bhanu V, Fydrych D, Pandey SM, Gupta A, Pandey C. Activated tungsten inert gas weld characteristics of P91 joint for advanced Ultra supercritical power plant applications. J Mater Eng Perform 2023. https://doi.org/10.1007
- [49] González-Velázquez JL. Fractography and failure analysis, vol. 3. Cham: Springer
- International Publishing; 2018. https://doi.org/10.1007/978-3-319-76651-5. [50] Pandey C, Mahapatra MM, Kumar P, Saini N. Effect of strain rate and notch geometry on tensile properties and fracture mechanism of creep strength enhanced ferritic P91 steel. J Nucl Mater 2018;498:176-86. https://doi.org/10.1016/j
- [51] Saini N, Pandey C, Mahapatra MM, Narang HK, Mulik RS, Kumar P. A comparative study of ductile-brittle transition behavior and fractography of P91 and P92 steel. Eng Fail Anal 2017;81:245-53. https://doi.org/10.1016/J ENGFAILANAL.2017.06.044.
- [52] Blach J, Falat L, Ševc P. Fracture characteristics of thermally exposed 9Cr-1Mo steel after tensile and impact testing at room temperature. Eng Fail Anal 2009;16: 1397-403. https://doi.org/10.1016/j.engfailanal.2008.09.003